7-13-2019

Modeling thermal and mechanical cancellation of residual stress from hybrid additive manufacturing by laser peening

Guru Madireddy
University of Nebraska- Lincoln

Chao Li
Autodesk Inc

Jingfu Liu
Sentient Science Corporation

Michael P. Sealy
University of Nebraska-Lincoln, sealy@unl.edu

Nanotechnology and Precision Engineering 2 (2019) 49–60

Contents lists available at ScienceDirect

Nanotechnology and Precision Engineering

journal homepage: http://www.keaipublishing.com/en/journals/nanotechnology-and-precision-engineering/

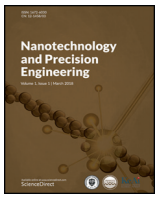

Modeling thermal and mechanical cancellation of residual stress from hybrid additive manufacturing by laser peening

Guru Madireddy [a], Chao Li [b], Jingfu Liu [c], Michael P. Sealy [a,*]

[a] Mechanical and Materials Engineering Department, University of Nebraska, Lincoln, NE, 68588, USA
[b] Autodesk Inc., 200 Innovation Blvd. Suite 208, State College, PA 16803, USA
[c] Sentient Science Corporation, 672 Delaware Avenue, Buffalo, NY 14209, USA

ARTICLE INFO

Available online 13 July 2019

Keywords:
Additive manufacturing
Laser peening
Finite element analysis
Residual stress
Hybrid

ABSTRACT

Additive manufacturing (AM) of metals often results in parts with unfavorable mechanical properties. Laser peening (LP) is a high strain rate mechanical surface treatment that hammers a workpiece and induces favorable mechanical properties. Peening strain hardens a surface and imparts compressive residual stresses improving the mechanical properties of a material. This work investigates the role of LP on layer-by-layer processing of 3D printed metals using finite element analysis. The objective is to understand temporal and spatial residual stress development after thermal and mechanical cancellation caused by cyclically coupling printing and peening. Results indicate layer peening frequency is a critical process parameter affecting residual stress redistribution and highly interdependent on the heat generated by the printing process. Optimum hybrid process conditions were found to exists that favorably enhance mechanical properties. With this study, hybrid-AM has ushered in the next evolutionary step in AM and has the potential to profoundly change the way high value metal goods are manufactured.

1. Introduction

A research area of critical importance identified by America Makes, NSF, NIST, the Department of Energy, CAM-IT, and others is material properties and subsequent performance of additive manufacturing (AM) parts.[1–6] Substandard properties and poor performance is a critical technical barrier to more widespread adoption of AM technology. High tensile residual stresses and cracking remain a major problem for the performance of additive manufactured components. Current practice to relieve residual stress typically involves heat treatments. Although heat treatments relax residual stress throughout the entirety of a part to prevent warping and cracking, key disadvantages include the following:

1) the ability to harden (*e.g.*, by grain boundary refinement, precipitation hardening, or martensitic transformation) are material/composition dependent and are not necessarily agreeable with additive manufacturing alloys;
2) heat treatments are not amenable to all materials; and
3) favorable compressive residual stresses are concurrently removed from a system along with the tensile residual stresses.

Another approach to delay cracking and wear in AM parts is to case harden a surface by peening, burnishing, nitriding, or carburizing. The primary disadvantage of these external surface treatments is the low penetration depth of hardening that ranges from a few microns to a few millimeters. Bulk mechanical properties remain unchanged. To improve service life of an AM part, an alternative manufacturing approach is needed that increases penetration depths beyond typical surface treatments. Therefore, this work proposes that heat treatments and surface treatments are the least desirable techniques to improve service life. An alternative solution is a hybrid additive manufacturing process chain that allows for control of work hardening and residual stress throughout the entire build volume of a component rather than the external surface only.

Hybrid additive manufacturing (hybrid-AM) processes have been defined as the use of AM with one or more secondary processes or energy sources that are fully coupled and synergistically affect part quality, functionality, and/or process performance.[7] One of the salient features of this definition is the fully coupled criterion that distinguishes pre- and post-processing of a build from those processes required *during* a build, often layer-by-layer (or multiples thereof). Synergy refers to the enhanced outcome(s) from coupling one or more secondary processes that is not achievable when uncoupled. Lastly, the third key feature relates to what experiences the enhanced outcome. In hybrid-AM processing, either the part, the process, or the part's functionality experiences the enhancement from fully coupling two or more

* Corresponding author.
E-mail address: sealy@unl.edu (M.P. Sealy).

https://doi.org/10.1016/j.npe.2019.07.001

processes. Secondary processes that have been coupled with AM include machining, laser reprocessing, and mechanical surface treatments.

Hybrid-AM using mechanical surface treatments, such as laser peening (LP), are of interest to bearing and tool and die applications due to the ability to work harden and impart favorable compressive residual stresses beyond the typical penetration depth of a surface treatment. Laser peening causes severe high strain rate plastic deformation from a shock wave that hardens and strengthens a surface. Consequently, fatigue life and wear resistance improve by delaying crack initiation and propagation. Coupling additive manufacturing with layer-by-layer laser peening is proposed as a novel approach to manipulate bulk mechanical properties that will improve the service life of parts.

In hybrid-AM, the primary AM process can be either directed energy deposition (DED), powder bed fusion (PBF), or sheet lamination. In DED, metal powder is blown into the melt pool created by a dense, high energy heat source (typically laser or electron beam) and deposited as a layer. In PBF, a scanning laser melts stationary powder particles to form a layer. Sheet lamination stacks sheets of metal that are bonded together using ultrasonic welding. It is important to note that the 3D mechanical properties achieved by coupling printing with laser peening are dependent on the AM process mechanics. In this paper, laser engineered net shaping (LENS®) was coupled with LP as a secondary layer-by-layer process. A schematic of LENS and LP is shown in Fig. 1.

There are new manufacturing challenges associated with coupling peening and 3D printing. Thermal and mechanical cancellation must be better understood for this approach to meaningfully impact the manufacturing industry. Thermal cancellation refers to the loss of favorable residual stress from heat. Mechanical cancellation refers to the loss of favorable residual stresses from undesirable stress redistribution.

In hybrid-AM, thermal cancellation occurs when a new layer is added on a peened surface (Fig. 2). The dashed and solid lines represent residual stress profiles after peening and after printing, respectively. The heat generated during material deposition has the potential to cancel any beneficial mechanical properties previously induced by peening. This phenomenon of eliminating or reducing the magnitude of favorable compressive residual stresses from the AM heat source is referred to as “thermal cancellation.” Naturally, thermal cancellation is dependent on AM process parameters and the corresponding heat entering the part. It is expected that the degree of sensitivity depends on the material being printed and its related thermal properties. Thermal cancellation in hybrid-AM is poorly understood.

Mechanical cancellation in hybrid-AM is the reduction of compressive residual stresses present below the surface due to application of peening on subsequent layers (Fig. 3). The dashed and solid lines represent residual stress profiles after peening different layers. Since peening induces both compressive and tensile residual stresses below the surface, peening new layers on top of previously peened layers redistributes residual stress fields. The tensile component of peening a new layer redistributes the compressive residual stress from peening a previous layer. The cumulative effects of coupling peened layers are poorly understood.

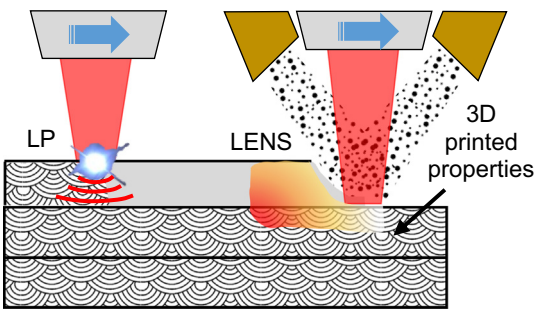

Fig. 1. Schematic of hybrid-AM using DED and laser peening.[7]

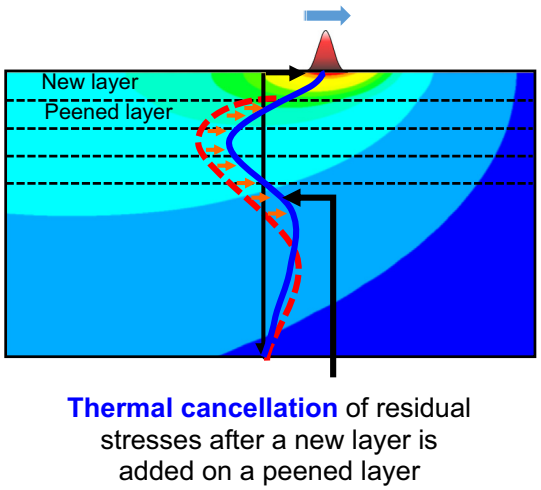

Fig. 2. Schematic representation of thermal cancellation of compressive residual stress caused by the heat from printing a new layer on top of a previously peened layer.[8]

The objectives of this paper are to introduce the concept of thermal and mechanical cancellation of residual stresses in hybrid-AM by laser peening and begin understanding the phenomenon through finite element analysis. A two-dimensional finite element model of hybrid-AM by laser peening was developed in ABAQUS to examine thermal and mechanical cancellation with varying layer peening frequency. Layer peening frequency refers to the cyclic cycle conveying the number of printed layers between peened layers. For example, a layer peening frequency of L5 indicates that every fifth layer was peened. The evolution of residual stresses from different layer peening frequencies and its effect on thermal and mechanical cancellation were studied.

2. Literature review

2.1. Modeling DED

According to ISO/ASTM 52900, DED is defined as an AM process in which focused thermal energy fuses materials by melting as layers are being deposited.[9] In DED, metal powder or filament is melted and deposited by focused thermal energy from a laser beam, electron beam, or plasma arc. Residual stress develops and evolves with the addition of layers that affects mechanical properties and subsequent

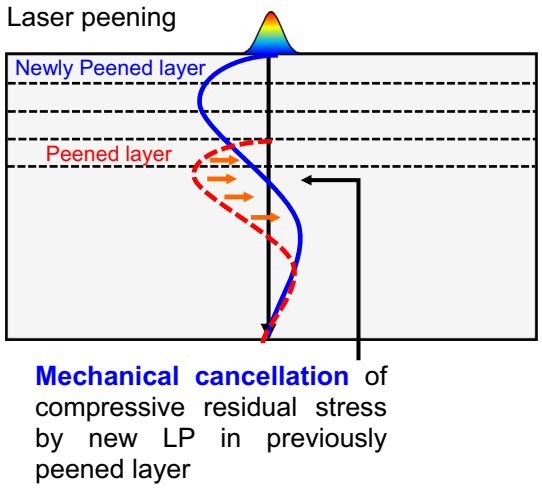

Fig. 3. Schematic representation of mechanical cancellation of compressive residual stress caused by peening a new layer on top of a previously peened layer.

performance. Modeling tools can be used to understand and predict residual stress development across different materials systems and machine platforms. The essential components needed to model DED include a moving thermal source (laser or electron beam), a technique for the addition of new layers, boundary conditions, and a temperature dependent material model. Investigators have modeled different types of DED processes including LENS®,[10–18] direct laser metal deposition (DLMD),[19,20] shape metal deposition (SMD),[21,22] and laser cladding.[23–25] The following sections describe techniques found in literature to model DED processes.

2.1.1. Heat flux

The thermal energy source during DED is modeled with a heat flux. Heat flux models are commonly used across multiple thermal processes, such as LENS®, laser cladding, laser metal deposition, and welding processes. The most common heat flux model is a Gaussian distributed function (Table 1). Pavelic first proposed this model for welding processes.[26] One advantage is the capability to adapt the melt pool by changing variables in the Gaussian function. The size of the melt pool is represented by a radius r. The constant c represents the effects of reflectivity, the beam distribution parameter, and the absorptivity of the material. For 3D models, the parameter r^2 changes to $r^2 = x^2 + y^2$.

Another common heat flux model is the double ellipsoid proposed by Goldak et al.[27] (Table 1). The main feature of this model is that it can be easily changed to represent both shallow penetration of an arc in welding and deeper penetration from laser and electron beam processes. The constants a, b, and c define the melt pool dimensions, and these values are different for front and rear ellipsoids. The constants depend on the specific heat source and material being modeled.

2.1.2. Material deposition

In order to model layer addition during DED, most researchers use one of two techniques: quiet element method and inactive element method.[10,12,16,20,24,28–31] In the quiet element method, unprinted elements are present in the model but assigned reduced material properties. These properties are obtained by multiplying with a scaling factor. Elements with reduced properties will not affect the analysis. As the analysis progresses and these quiet elements are ready to be "printed," realistic material properties are assigned to quiet elements in order to establish their presence in the model. Inactive element is another approach that is similar to the quiet element method. However, the difference is that deposited elements are deactivated at beginning of the analysis. Elements are activated in each step individually (or as a layer) as the heat source acts upon that layer.

Table 1
Heat flux (Q) models.

Heat flux equations		Ref.
$Q = \frac{cP}{\pi r_0^2} e^{-\left(\frac{2r^2}{r_0^2}\right)}$	Gaussian heat flux distribution function	[10–18]
where, c = absorption coefficient P = laser power r_0 = initial radius r = current radius		
$Q = \frac{6\sqrt{3}\,P\eta f}{abc\,\pi\sqrt{\pi}} e^{-\left[\frac{3x^2}{a^2}+\frac{3y^2}{b^2}+\frac{3(z+v_w t)^2}{c^2}\right]}$	Double ellipsoid model as laser heat source	[12,21,22,28,29]
where, P = laser power η = absorption efficiency f = process scaling factor a = transverse dimension of ellipsoid b = depth of melt pool c = longitudinal dimension of ellipsoid t = time v_w = heat source travel speed		

2.1.3. Thermal boundary conditions

In DED, it is important to have boundary conditions to accurately calculate temperatures developed in layers during material deposition. These boundary conditions influence the amount of heat passing through the system and will influence the amount of residual stress and distortion present in a part. Boundary conditions depend on the type of DED process. For example, electron beam melting takes place in a vacuum, where heat transfer occurs only through conduction in the material and radiation on the surface of the build.[28] Whereas in processes such as LENS®, laser cladding, and DLMD, powder material is blown into the melt pool through inert gas. The flow of inert gas over the melt pool acts as forced convection. Most thermal models in literature have both convective and radiative heat transfer conditions on all surfaces.[11,12,18–20,22–24,29–32] Beuth et al. did not include the convective or radiative heat transfer conditions while modeling LENS® to build 2D thin wall structures.[17,33] Dobranich and Dykhuizen suggested thermal results near the heat source were not significantly affected when the boundary conditions along vertical edges and the top surface were specified as either convective or insulated.[34] Another boundary condition to be considered is heat transfer from deposited layers to the substrate below. Usually, most models use a fixed temperature on the bottom surface as a boundary condition. To include heat conducted into a substrate, Chiumenti et al. applied a convective coefficient to the bottom boundary of a numerical model.[16]

2.1.4. Material models

Due to the thermal characteristics of DED, temperature-dependent properties of a material should be incorporated into the simulation. These temperature-dependent properties account for phase transformation, melting, and re-solidification of the material. The transformation of material from liquid phase to solid phase can be defined by latent and specific heat, respectively. Most researchers used temperature dependent thermal conductivity, specific heat, and density.[16,18,19,33] Other mechanical properties, such as a temperature dependent elastic modulus or thermal expansion, are used to determine stresses and deformations developed in a model due to deposition.

2.2. Modeling laser peening

2.2.1. Loading conditions

When the laser interacts with the surface, plasma forms and continues to absorb laser energy. Part of this energy is released into the surface as a pressure wave. To simplify laser-material interactions, laser peening is modeled as a pressure wave that is a function of both radial distance and peening time as follows[35,36]:

$$P(r,t) = P(t)\,\exp\left(-\frac{r^2}{2R^2}\right) \quad (1)$$

where $P(t)$ is the magnitude of pressure at any time, r is the radial distance from the center of the spot, and R is the spot size. Each of these parameters affects the compressive residual stresses induced in the material. For example, Peyre et al. observed that with increase in the laser spot size, the depth of compressive residual stresses increases substantially without a significant difference in magnitude.[37]

The pressure-time history is defined using the Gaussian temporal profile with a short rise time.[38–42] Braisted and Brockman used a triangular pulse because of a very narrow pulse duration on the order of several nanoseconds[43] (Fig. 4). Since the spatial and temporal pressure distributions during LP are neither uniform nor linear, a subroutine DLOAD/VDLOAD can be used to apply the non-uniform shock pressure.[36,44] This subroutine allows the pressure to vary with respect to both the radius of the laser spot and time.

2.2.2. Material models

The most common material model to capture high strain rate behavior is Johnson-Cook (JC). The expression for equivalent stress for a given temperature T is given by

$$\sigma_{eq} = \left(A + B\varepsilon_{eq}^{n}\right)\left[1 + C\ \ln\left(\frac{\dot{\varepsilon}}{\dot{\varepsilon}_0}\right)\right]\left[1 - \left(\frac{T - T_0}{T_{melt} - T_0}\right)^{m}\right] \quad (2)$$

where T_0 is the reference temperature, T_{melt} is the melting temperature of a material, ε_{eq} is the equivalent plastic strain, $\dot{\varepsilon}$ is the plastic strain rate, $\dot{\varepsilon}_0$ is the plastic strain rate in a quasi-static state of the material, and A, B, C, n, m are the material constants. The JC model calculates flow stress in the material considering independent effect of strain hardening, strain rate, and temperature while ignoring the interdependency of the terms.

Bammann et al. developed an internal state variable (ISV) plasticity model for high strain rate-, temperature-, and hardening-dependent constitutive relations.[46–48] This constitutive model is capable of predicting deformation and failure in a material. LP requires a material model that accounts for a dynamic yield stress. A material user subroutine (UMAT/VUMAT) developed at Mississippi State University was incorporated into ABAQUS. Below are the corresponding constitutive equations.

$$\dot{\sigma}_{-} = \lambda \mathrm{tr}(D_{-}^{e})I_{-} + 2\mu D_{-}^{e} \quad (3)$$

$$D_{-}^{e} = D_{-} - D_{-}^{p} \quad (4)$$

$$D_{-}^{p} = f(T)\ sinh\left[\frac{\|\sigma_{-} - \alpha_{-}\| - \{R + Y(T)\}}{V[T]}\right]\frac{\sigma_{-} - \alpha_{-}}{\|\sigma_{-} - \alpha_{-}\|} \quad (5)$$

$$\dot{\alpha}_{-} = h(T)D_{-}^{p} - \left[\sqrt{\frac{2}{3}r_d(T)\|D_{-}^{p}\| + r_s(T)}\right]\|\alpha_{-}\|\alpha_{-} \quad (6)$$

$$\dot{R} = H(T)D_{-}^{p} - \left[\sqrt{\frac{2}{3}R_d(T)\|D_{-}^{p}\| + R_s(T)}\right]R^2 \quad (7)$$

where σ_{-} is the flow stress which is a function of elastic strain D_{-}^{e}. The plastic rate of deformation D_{-}^{p} depends on the hardening functions, recovery functions, and yield functions. These functions are defined as temperature dependent to evaluate the interdependency of strain, strain rate, and temperature on the flow stress of the material.

3. Finite element modeling of hybrid-AM

3.1. Model description

The two-dimensional model developed for simulation is shown in Fig. 5. A total of 20 layers were deposited on the substrate, each 30 mm wide and 0.3 mm thick. The substrate below the layers had dimensions of 30 mm by 8 mm. The elements in the thermal model were the DC2D4 type, which represents 4-node diffusive conductive heat transfer elements used to evaluate temperatures developed during the application of a moving heat source. Whereas, the elements in the stress models were CPE4, which represents 4-node bilinear plane strain elements that captured stresses due to the heat source and the application of laser peening. The element size in the layers was 20 μm by 20 μm, and a gradient size was given to elements in the substrate to minimize computational time. The addition of material during AM was simulated by means of the successive discrete activation of a new set of elements in the model at the beginning of each step (*i.e.*, inactive element method).

3.2. Material model

AISI 52100 steel was considered for this simulation for its wide usage in transportation bearings and availability of model constants. In heat transfer analysis, thermo-physical properties were used to evaluate temperatures and can be found in Appendix A. In stress analysis without LP, temperature-dependent elastic and plastic properties (Young's modulus, Poisson's ratio, yield strength) were given along with the temperature-dependent thermal expansion of the material. The plastic properties were provided by,[50] and the yield strength was set artificially low above the vaporization temperature. For the stress analysis with LP, internal state variable model (ISV model) was used.

3.3. Loading and boundary conditions

3.3.1. Heat transfer analysis

A moving heat flux was applied to simulate the temperatures developed in the DED on each layer. The heat flux was modeled as a non-uniform distributed flux as a function of position and time. The heat flux given by the equation below follows Gaussian distribution and was modeled using the ABAQUS user subroutine DFLUX.

$$q = \frac{CP}{\pi r^2} e^{\frac{-2(x - vt)^2}{r^2}} \quad (8)$$

where C is the absorption coefficient, P is laser power in watts, r is the radius of the laser beam in meters, v is scanning speed of heat flux in m/s. LENS® process parameters that were used to simulate the AM process are given in the table below.

Thermal boundary conditions including conduction, convection, and radiation were applied to the model. A thermal conduction coefficient (k) was provided for heat transfer between layers. The heat conducted into the substrate was given in terms of convection at the bottom of the substrate ($h_3 = 1000$ W/(m^2·K)). A forced convection and radiation heat transfer boundary conditions were given on the top surface of each

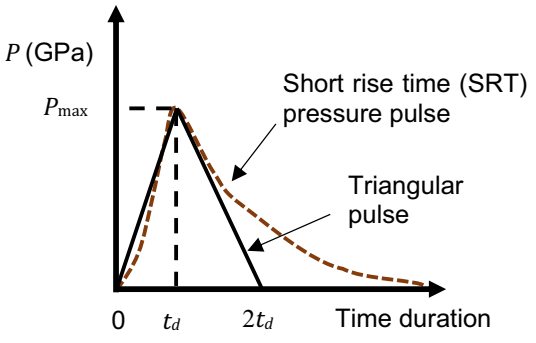

Fig. 4. Pressure-time profile of single LP.[45]

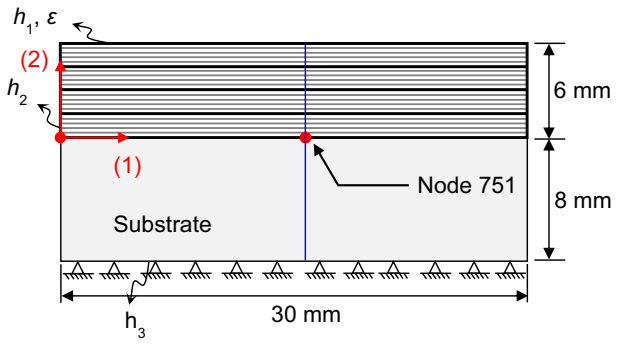

Fig. 5. Schematic of hybrid-AM model with thermal and mechanical boundary conditions.

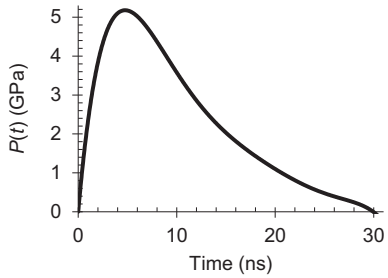

Fig. 6. Variation of pressure with respect to time.

layer while depositing ($h_1 = 100$ W/(m^2·K), $\varepsilon = 0.62$) to account for heat transferred through inert gas blown into the melt pool and through radiation to the surrounding environment. Free convection to the surrounding environment was given as a boundary condition on the edges of layers and substrate ($h_2 = 25$ W/(m^2·K)).

3.3.2. Stress analysis

The pressure wave from LP was modeled as a function of radial distance and peening time. The LP process parameters are provided in Table 3. The process parameters were chosen to achieve the maximum possible penetration depth of compressive residual stress before reaching a saturation point. The pressure varying with peening time follows a short rise time pulse as shown in figure below. It was assumed that the pressure duration was three time longer than pulse duration and glass was used as confining layer. Under these assumptions, a peak pressure of 5.17 GPa was applied during laser peening to induce compressive residual stresses into the material. The load was applied on material for 30 ns in loading step and was allowed to relax for 10^{-4} s. The variation of stresses with time is shown below (Fig. 6).

3.4. Simulation procedure

A commercial finite element software ABAQUS/Standard was used to simulate hybrid-AM by DED and laser peening. The simulation procedure is shown in the flow chart (Fig. 7) below. To simulate this process, two models of identical geometry were developed: one model for heat transfer analysis with DC2D4 elements and the other for stress analysis with CPE4 elements. In the heat transfer analysis, temperatures developed during DED were computed and imported to a stress analysis. The stresses from the temperatures and LP were determined using static/general stress analysis.

In hybrid-AM by laser peening, a heat transfer analysis was developed first. The temperatures developed in the heat transfer analysis were exported to the stress analysis to calculate stresses from temperatures. Then in laser peening analysis, the stresses from adding layers were imported as initial conditions, and laser peening was applied completing the first peening cycle. In the next cycle, another set of layers was added in the heat transfer analysis, and stresses from those temperatures were calculated with stresses from the previous laser peening as initial conditions followed by a laser peening analysis. The same cycle was repeated until all layers were printed.

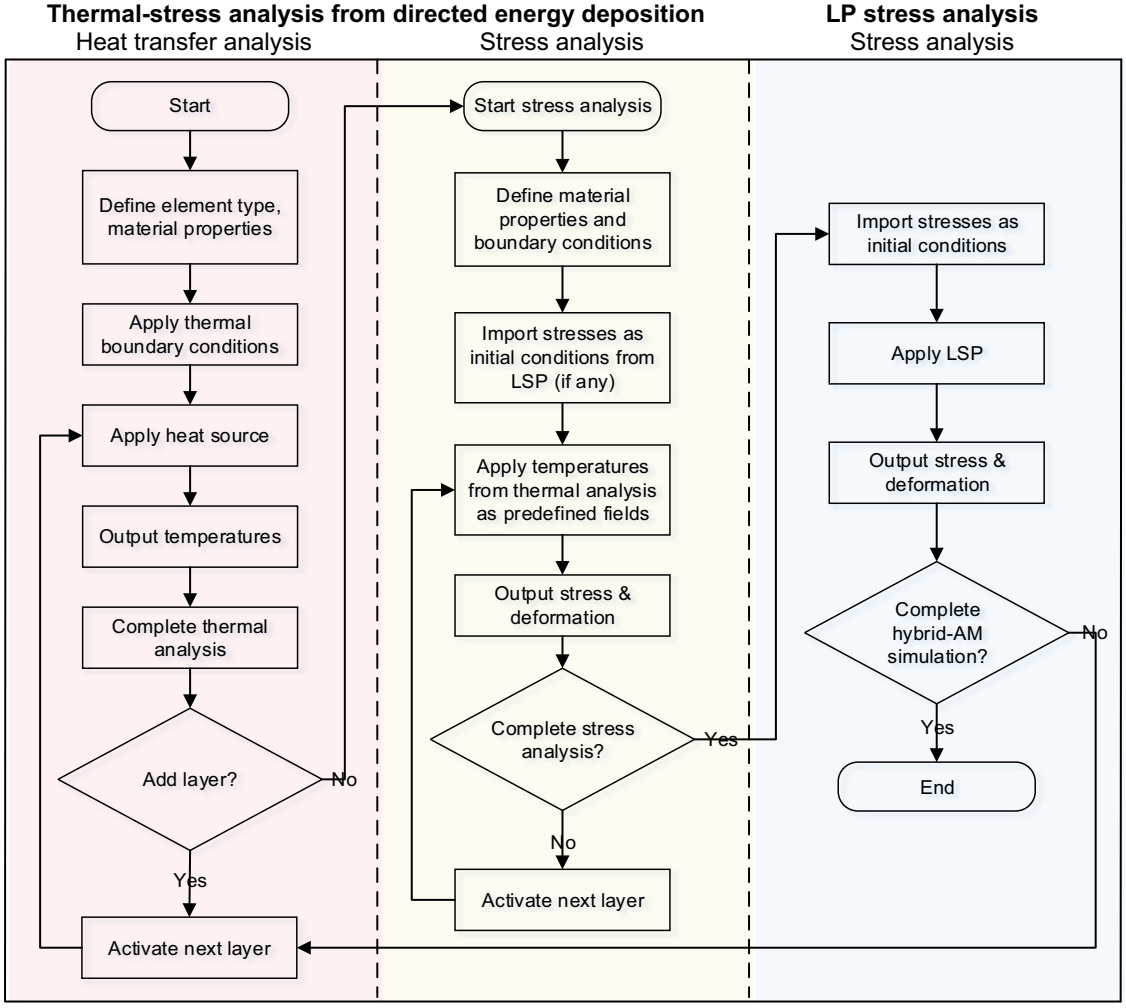

Fig. 7. Flow chart for simulation procedure of hybrid-AM by laser peening.

Table 2
Heat flux process parameters.

Laser power (W)	Laser spot size (mm)	Scan speed (mm/s)	Scan length (mm)
400	1.36	10	30

3.4.1. Case study (hybrid L5)

To explain the simulation procedure, a case study was done with laser peening on every fifth layer (number of printing layers in each cycle = 5) until twenty layers were deposited. In this simulation, there were four cycles/iterations. Each cycle contained a heat transfer analysis, a stress analysis, and a laser peening analysis. In the first heat transfer analysis, layers 1–5 were added one-by-one and heat flux was applied on each layer to incorporate temperatures generated in an AM process. These temperatures were exported to a stress analysis of five printed layers to compute stresses. Then, the stresses generated by adding 1–5 layers in the AM process were imported to a laser peening analysis as the initial conditions. In the laser peening analysis, a single laser peening was applied on the fifth layer and stresses developed were computed. This completed one of the four cycles of the hybrid-AM process.

In the second heat transfer analysis, layers 6–10 were added one-by-one with heat flux applied on each layer. Then, similar to the previous stress analysis, the temperatures were imported to evaluate stresses developed, but here along with temperatures, stresses were also imported from the previous laser peening analysis as initial conditions. This was to determine the effect of the addition of new layers on a laser peened surface in terms of residual stresses. The stresses from stress analyses of 1–10 printed layers were imported as initial conditions and laser peening was applied on the tenth layer inducing compressive stresses. This completed the second cycle.

Similarly, layers 11–15 were added in the third cycle and stresses were calculated by importing temperatures as predefined fields and stresses from the second laser peening as initial conditions. Laser peening was applied on the fifteenth layer. Likewise, the final set of layers was added, and stresses were computed.

4. Results

In this paper, five simulations were developed: as-built (no laser peening), laser peening on the surface only (surface peened), laser peening on every 10 layers (hybrid L10), laser peening on every 5 layers (hybrid L5), laser peening on every layer (hybrid L1). These five cases were compared to determine the effect of layer peening frequency on the stress distribution in layers. All the cases were modeled with AISI 52100 as the material, and with AM parameters mentioned in Table 2 and LP parameters in Table 3.

4.1. Final residual stresses

The final residual stresses in direction-1 along the depth for all the models are shown below (Fig. 8). A full residual stress field map is shown in Fig. 9 for each condition. The "As-Built" condition represents the stress model of the DED process without any LP. From the plot (Fig. 8), it was observed that the stresses in layers were tensile because of the continuous application of heat flux on the layers. This continuous heat flux allowed the material to expand and induce tensile residual stresses in the layers. The magnitude of the stresses in layers varies from 600 MPa to 1325 MPa.

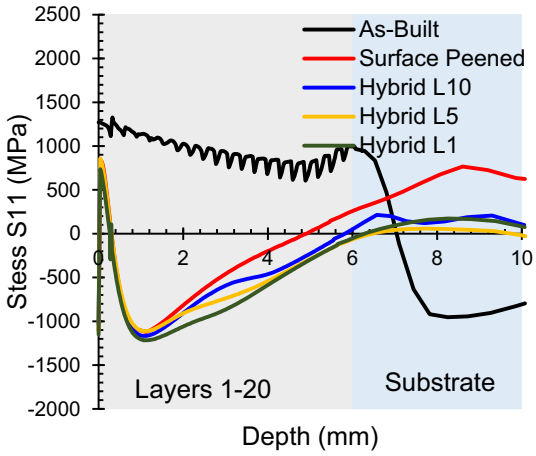

Fig. 8. Stress profiles comparison of hybrid-AM models.

The stress variation with depth from single laser peening applied on the surface after twenty layers, *i.e.*, "Surface Peened", was modeled for comparison to hybrid conditions. In this case, peening was not fully coupled; rather, peening was sequentially coupled as a traditional surface treatment. The tensile stresses from adding layers turned compressive and reached a peak of −1120 MPa. The compressive residual stresses from single laser peening penetrated 4.9 mm before turning tensile. Three hybrid conditions at different peening frequencies were examined. The depth of compressive residual stress increased as the peening frequency increased from every ten layers (5.8 mm) to every five layers (6.5 mm). A saturation point was reached such that further increasing the peening frequency to every layer decreased the depth to 6.3 mm. Although a saturation point was reached, higher layer peening frequency increased the width of the compressive residual stress region. The magnitude of peak compressive stress for all cases ranged between −1120 MPa to −1220 MPa.

As the stress variation along a line at the center of the model does not represent the entire stress distribution, Fig. 9 shows the stresses in different models. To quantify the residual stress distribution, the width and depth of compressive residual stresses (blue regions in Fig. 9) higher than −650 MPa were measured and provided in Table 4. It was observed that as the peening frequency increased, the width and depth of residual stress regions increased. That is, more frequent peening resulted in a more sustained compressive residual stress band below the surface.

4.2. Temperature history

Thermal history of a model is crucial for residual stress evolution in the material. Temperatures generated during layer addition stimulate thermal cancellation of compressive residual stresses developed from laser peening. While modeling the DED process, the heat flux was applied on each layer to simulate temperatures developed during printing. The temperatures experienced within previously added layers vary as new layers are deposited. The node 751 (shown in Fig. 5) was selected

Table 3
LP process parameters.

Pressure duration (ns)	Spot size (mm)	Peak pressure (GPa)	Pulse duration (ns)	Laser intensity (GW/cm^2)	Laser power (J)
30	2.25	5.17	10	3.59	1.42

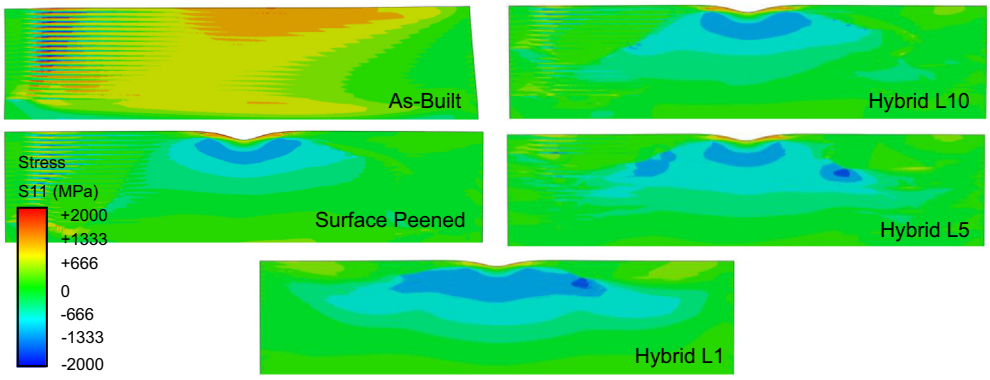

Fig. 9. Residual stresses developed in layers in each model.

Table 4
Size of the compressive residual stress region greater than −650 MPa.

Model	Width (mm)	Depth (mm)
As-built	n/a	n/a
Surface peened	12.2	2.5
Hybrid L10	15.3	2.6
Hybrid L5	16.5	3.2
Hybrid L1	22.1	3.7

at the top of the substrate to understand the variation of temperatures. At this position, the temperatures from adding all 20 layers was calculated, and the temperature variation was plotted with respect to time as all 20 layers were added (Fig. 10). As the first layer was being added, the peak temperature on top of the substrate reached 2700 K. For the second layer, the temperature observed at the node was 1544 K, *i.e.*, as one layer was added, the layer below it experienced near melting temperatures. As the layers added, the peak temperature experienced by the node decreased exponentially. Temperatures above the transition temperature (approximately 820 K) would affect microstructure. The temperature of the node was above the transition temperature until the seventh layer (L7) was added. When the eighth layer was added, the temperature dropped below transition temperature (778 K). This indicated the heat flux from adding a new layer affected the microstructure of the seven layers below it. Although the microstructure was not modeled in this paper, this is very important in terms of stress evolution in hybrid-AM process.

4.3. Hybrid L10

In hybrid L10, the stress development/redistribution in layers were plotted along the depth as layers were added (Fig. 11).

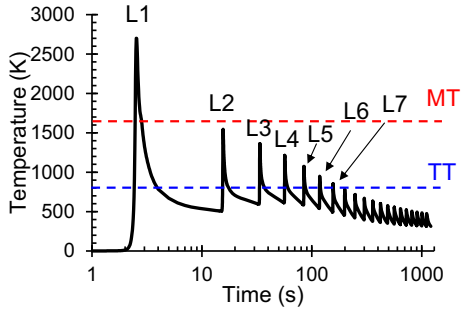

Fig. 10. Temperature profile with time at top center of substrate (MT-melting temperature, TT-transition temperature).

The stress profile is represented as a solid line when adding a new layer (L10 represents stresses after addition of ten layers), and the laser peened layer is represented with a dotted line (Peening Layer 10: stress profile after printing and laser peening on 10th layer).

In Fig. 11a, the L10 curve represents stresses in layers after ten layers were printed. The L10 curve is similar to the as-built in Fig. 8, and the maximum tensile stress developed in the layers was 1900 MPa. Peening layer 10 in Fig. 11b represents the stress profile after laser peening the tenth layer. From this curve, it was observed that all the tensile stresses present in ten layers turned compressive after the tenth layer was laser peened, and the peak compressive stress was −1110 MPa. Then, a new layer (L11) was added on the laser peened layer (*i.e.*, the 10th layer). Here, an interesting process phenomenon was observed. In the newly added layer (L11), tensile stresses were developed as expected from the AM process; however, the peak compressive stress reduced from −1100 MPa to −490 MPa in the laser peened layer below it (10th layer). This reduction in compressive stresses when a new layer was added on the laser peened layer is termed as “thermal cancellation” (Fig. 11b). This was due to the heat conducted from layer 11 to layer 10 during printing and caused an expansion and redistribution of compressive stresses in layer 10.

In the next step, the 12th layer was added. Similar to the previous layer (11th layer), tensile stresses were developed in L12; however, the compressive stresses increased from −490 MPa to −590 MPa in the previous laser peened layer (Fig. 11b). This increase in compressive stress in the laser peened layer due to the addition of new layers is termed “thermal addition.” This may be attributed to the stress redistribution during the DED process. As-printed layers have high tensile stresses. To compensate, compressive stresses are induced in layers below the printed layer. After all layers were added, there was a peak tensile stress of 1660 MPa in the newly added layers 11–20 and peak compressive stress of −938 MPa was observed in previously peened layer (10th layer). This implies there was an increase of −448 MPa in the 10th layer due to thermal addition. Next, another laser peening was applied on layer 20. This laser peening induced a peak compressive stress of −1170 MPa. Another interesting phenomenon observed here was that the magnitude of compressive stress in the 10th layer decreased from −938 MPa to −456 MPa after 20th layer was peened. This reduction in compressive stress in layer 10 after the 20th layer was laser peened is called “mechanical cancellation.” This may be due to the hook shape development of the stress profile from laser peening. This shape of residual stress profile from laser peening makes the stresses go tensile after a certain depth. As there exist compressive stresses in the 10th layer, the new laser peening on the 20th layer increased the depth of compressive residual stresses. This may be the reason why the depth of compressive stresses in hybrid L10 model was 6.25 mm while it was 4.9 mm in surface peened model.

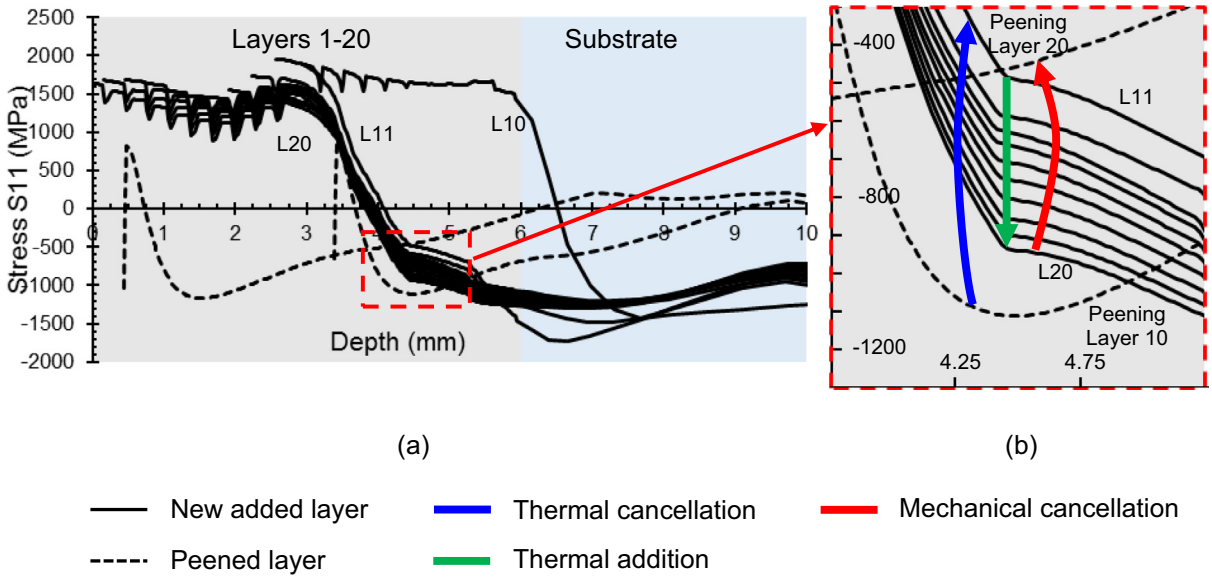

Fig. 11. Stress profile evolution of hybrid-AM model with laser peening on every 10 layers.

4.4. Hybrid L5

In this case, five layers were printed and laser peening was applied on top of the 5th layer. Next, another five layers were added, and laser peening was applied on 10th layer. The process was repeated until all 20 layers were added. Fig. 12 shows stress profile evolution along the depth as the new layers were added on a peened surface.

The curve L5 in Fig. 12a represents the stress profile after adding five layers. When the LP was applied on the 5th layer, the tensile stresses present in layers 1–5 turned compressive. In the next step, the 6th layer was added, and stresses in the 6th layer were tensile as expected; however, the magnitude of compressive stresses in the previously peened layer increased (Fig. 12a). Instead of thermal cancellation as observed in the hybrid L10 model, thermal addition made the stresses more compressive at this depth. This thermal addition continued until the 10th layer was added. When LP was applied on the 10th layer, mechanical cancellation was observed (Fig. 12a). A similar trend of thermal addition and mechanical cancellation were observed for the next cycle:

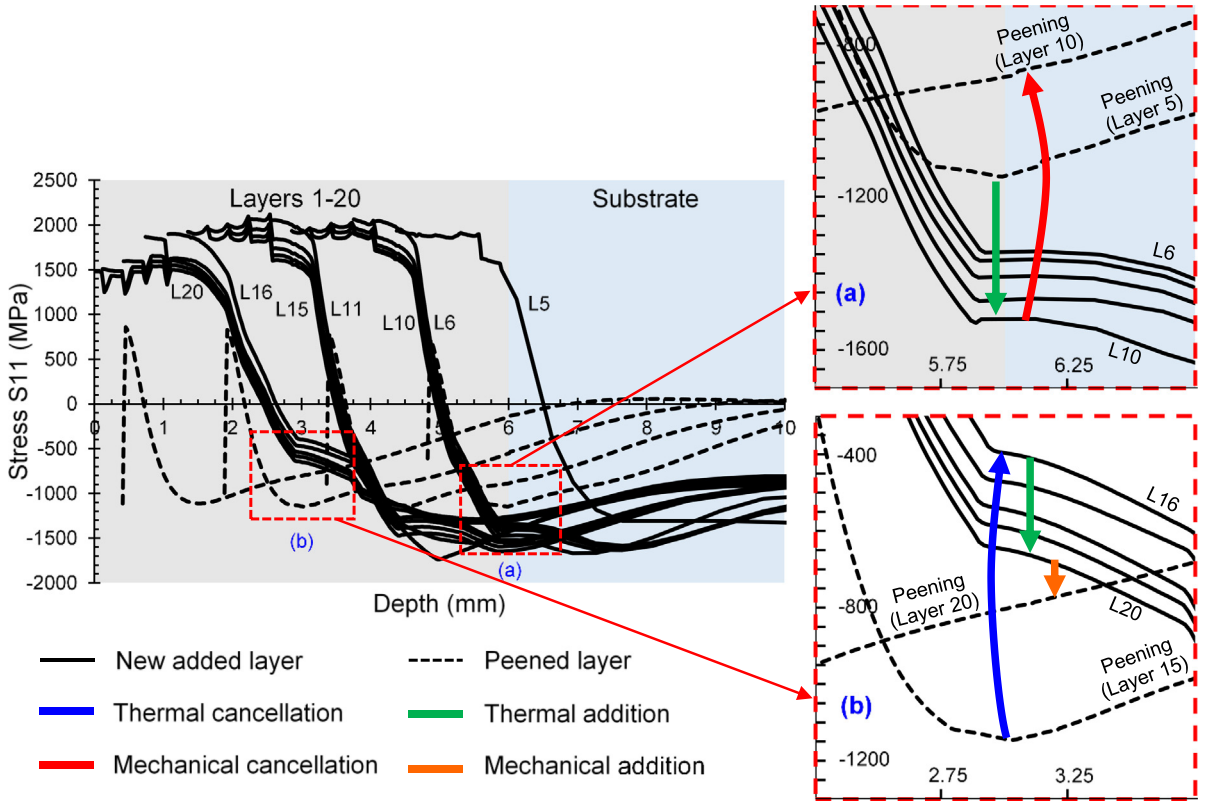

Fig. 12. Stress profile evolution of hybrid-AM model with laser peening on every 5 layers.

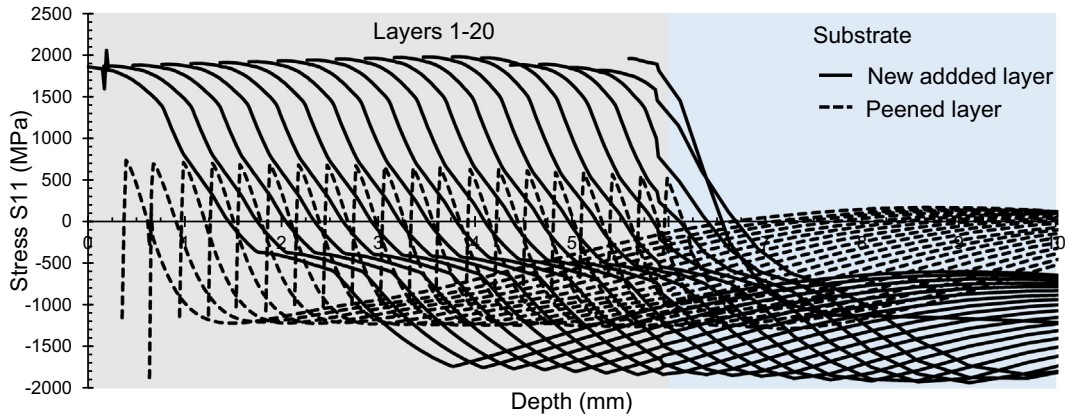

Fig. 13. Stress profile evolution of hybrid-AM model with laser peening on every layer.

adding layers 11–15 and LP on 15th layer. In the next step, the 16th layer was added inducing thermal cancellation in the previous peened layer followed by thermal addition as the layers were being added until layer 20. Laser peening was applied on the 20th layer. Instead of mechanical cancellation, mechanical addition was observed in the laser peened layer (layer 15). When laser peening was applied on the 20th layer, instead of mechanical cancellation as seen in the previous cycles (L1–5, L6–10, L11–15), "mechanical addition" was observed (Fig. 12b). Mechanical addition is defined as the addition of compressive stresses in previously peened layers when a newly added layer in the AM process was peened.

4.5. Hybrid L1

In this case, laser peening was applied after the addition of each layer in DED. When a new layer was added on a peened surface, the compressive stresses in the previous peened layers decreased. That is, thermal cancellation was observed. After LP, compressive stresses increased in the previous peened layers, *i.e.*, mechanical addition was observed. The same cycle of thermal cancellation and mechanical addition was observed for all 20 layers. This stress evolution is plotted below (Fig. 13).

4.6. Step history evolution of stresses

All the plots until this point are local time histories and the stress variation with respect to depth in different models. However, the step histories of these models convey more information on residual stress reversal. Each step corresponds to the addition of a new layer or laser peening of a layer. For example, hybrid L5 model has 20 layers added and LP was applied on layers 5, 10, 15, and 20; so this model will have a total of 24 steps with LP at steps 6, 12, 18, and 24. Similarly, the models surface peened, hybrid L10, and hybrid L1 have 21, 22, and 40 steps respectively. To observe the stress variations, element 44,250 was selected, which is at the top center of the substrate. In Fig. 14, the red colored circles indicate the stress value after the addition of a new layer, and the blue colored circle indicates the stress value after a particular layer was peened. In surface peened model (Fig. 14a) where no LP was applied in between the layers, the stress had minimal variation until peening on the 20th layer in step 21. At this step, the stress was reduced from 993 MPa to 136 MPa, a decrease of 857 MPa. In the hybrid L10 model, the stress was tensile until LP was applied on layer 10 decreasing the stress by 2.1 GPa. Beginning with the addition of layer 11, as the new layers were added, the stresses stayed compressive and ranged from −1.4 GPa to −1.2 GPa until another LP was applied changing the stress from −1.2 GPa to −75 MPa. In the hybrid L5 model, the stress variations at the peened steps were 2.6 GPa, −650 MPa, −1.1 GPa, and − 1.5 GPa. In the hybrid L1 model, after the addition of the first layer, the stress was approximately 1900 MPa. After LP was applied on it, the stress dropped to −200 MPa, *i.e.*, with the application of LP there was a change in stress of 2.1 GPa. Similarly, the change in stress varied from 2.1 GPa to a few hundreds of megapascals as the first 10 layers were added. Until this point, the newly added layers induced tensile stresses while LP induced compressive stresses. After the addition of the 11th layer, this trend was reversed. That is, after the addition of layer 11, printing new layers induced compressive stresses and the stresses due to peening became tensile. This trend continued until all the remaining layers were added and peened. These variations in stresses from tensile to compressive or *vice versa* can be observed in all the models developed in this paper. The large reversals in stresses were due to the stress redistributions during the thermal and mechanical cancellations.

5. Summary and conclusions

From the 2D finite element model of hybrid-AM by DED and LP, it was shown that layer-by-layer peening during additive manufacturing (AM) induced compressive residual stresses in the workpiece that were not completely cancelled from heat or mechanical redistribution. Critical hybrid process parameters were identified, such as layer peening frequency, peening intensity (includes laser power and spot size), and layer thickness. It was shown that decreasing layer peening frequency (*i.e.*, peening more frequently) from 20 to 5 increases the depth of compressive residual stresses (CRS). In this case study where the layer thickness was 0.3 mm, the depth of CRS saturated below a peening frequency of every 5 layers. That is, peening more frequently than every five layers did not increase the depth of CRS. In single peening mode, the peak CRS below the surface was similar (± 100 MPa) for all layer peening frequencies. Interestingly, the width and thickness of the CRS, referred to as the CRS band, increased with more frequent layer peening. Peening every layer had the widest and thickest CRS band. Based on these results, it is hypothesized that peening fewer layers with multiple peenings would be equivalent to peening every layer with a single peening. Multiple peenings should increase the width and thickness of the CRS band.

The stress profile evolution in the model with a layer peening frequency of ten exhibited thermal cancellation, thermal addition, and mechanical cancellation. When peening every 5 layers, in layers 5 and 10, thermal addition and mechanical cancellation were observed. In layer 15, thermal cancellation and mechanical addition were observed. No mechanical cancellation was observed when peening every layer. This may be due to the high peening frequency. The depth of the peak CRS from peening layers reached the previously peened layers below and

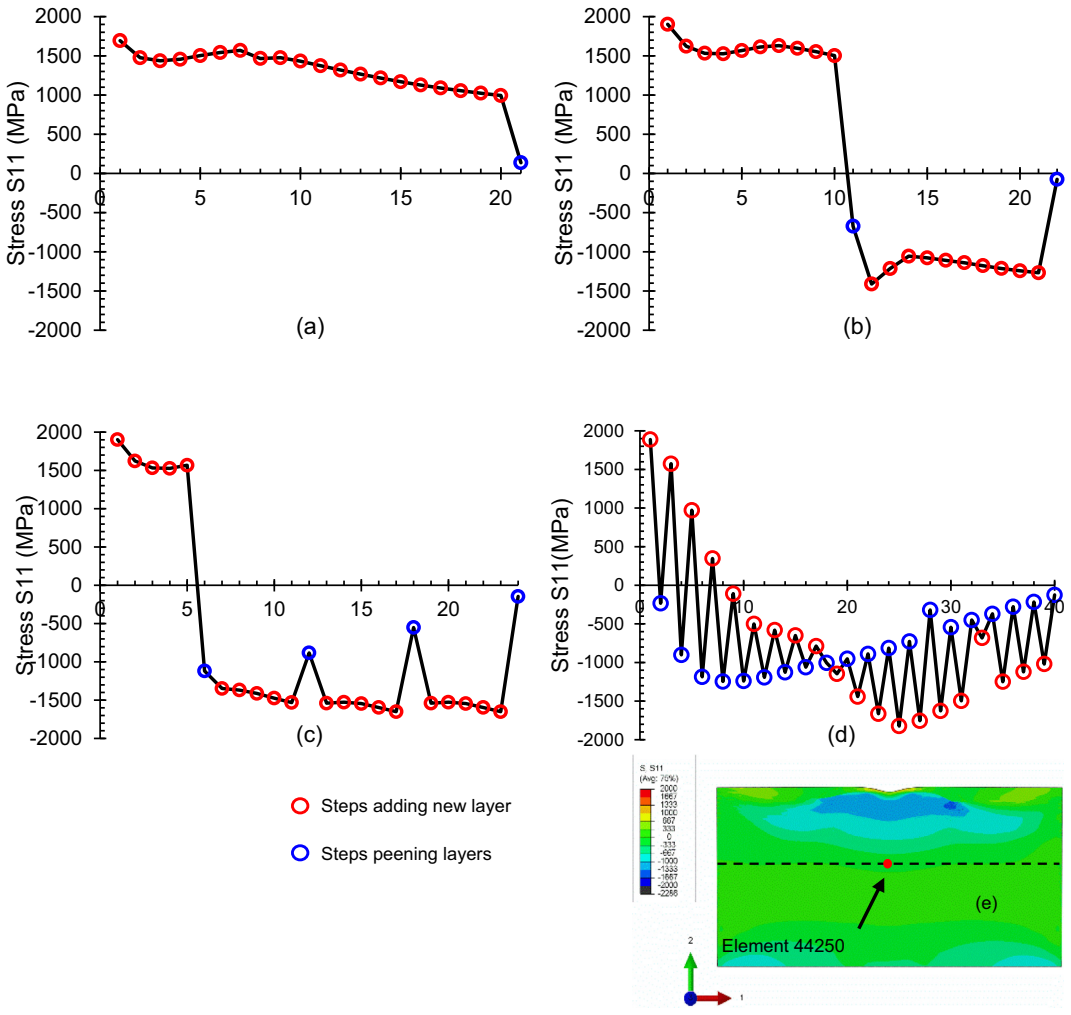

Fig. 14. Step history of residual stresses at element 44,250 in (a) surface peened, (b) hybrid L10, (c) hybrid L5, (d) hybrid L1 models, and (e) location of element 44,250 at the interface of the baseplate and build.

resulted in an increased CRS. This indicates complex residual stress histories exist that are dependent on the location in the workpiece. Understanding these histories may be important in designing for performance. In steels, the reversals in stress from thermal and mechanical cancellation ranged from 100's of megapascals to a few gigapascals. Hybrid processing of a steel may result in short cycle fatigue failure when coupling printing and peening because of the dramatic reversals in CRS.

Acknowledgements

This research was supported by in part by the National Science Foundation through the awards CAREER #1846478 and STTR #1521188.

Appendix A. Material properties of AISI 52100

Table A.1

Physical properties of AISI 52100.

Latent heat of fusion	(kJ/kg)	276
Latent heat of vaporization	(kJ/kg)	6290
Melting point	(K)	1640
Boiling point	(K)	2750
Density	(kg/m^3)	7827

Table A.2
Temperature dependent thermal expansion.[49]

Thermal expansion (μK^{-1})	Temperature (K)
11.5	298
12.6	477
13.6	671
14.9	977
15.3	1077

Table A.3
Temperature dependent elastic properties.[50]

Young's modulus (GPa)	Poisson's ratio	Temperature (K)
201.33	0.277	295
178.58	0.269	473
162.72	0.255	673
103.42	0.342	873
86.87	0.396	1073
66.88	0.490	1273

Table A.4
Temperature dependent plastic properties.[50]

Yield stress (MPa)	Plastic strain	Temperature (K)
1600	0	293
1900	0.002	293
2000	0	493
2300	0.025	493
1180	0	693
1220	0.045	693
20	0	5000
23	0.02	5000

Table A.5
ISV constants for AISI 52100.[51]

Material constants		
Shear modulus (G)	(MPa)	78,500
a		1.23
Bulk modulus (K)	(MPa)	152,000
b		−1.85E10
Melting point	(K)	1640
C_1	(MPa)	1
C_2	(K)	1
C_3	(MPa)	1070
C_4	(K)	58.5
C_5	(1/s)	1
C_6	(K)	−12,000
C_7	(1/MPa)	0.04
C_8	(K)	0
C_9	(MPa)	5600
C_{10}	(MPa/K)	9
C_{11}	(1/MPa)	0.002385
C_{12}	(K)	400
C_{13}	(1/MPa)	0.05
C_{14}	(K)	0
C_{15}	(MPa)	150
C_{16}	(MPa/K)	−14
C_{17}	(MPa/s)	0.0027
C_{18}	(K)	0
C_{19}	(1/K)	0.004148
C_{20}	(K)	665
Initial temperature	(K)	293
Heat coefficient	(m^3·K/J)	2.43E−07
Initial damage		0.01
Damage exponent		3

Table A.6
Temperature dependent specific heat.[49]

Specific heat (J/(kg·K))	Temperature (K)
458	300
640	473
745	699
798	810

Table A.7
Temperature dependent conductivity.[52]

Conductivity (W/mK)	Temperature (K)
37	273
41	373
40	473
38	573
36	673
34	773
33	823
32	883
30	923
29	973
25	1023
25.5	1173

References

1. Huang Y, Leu MC, Mazumder J, Donmez A. Additive manufacturing: current state, future potential, gaps and needs, and recommendations. J Manuf Sci Eng 2015;137. (p. 014001:1-10).
2. Advanced Manufacturing Office. *Additive manufacturing: pursuing the promise*. U.S. Department of Energy (DOE. 2012, www.manufacturing.energy.gov.
3. National Institute of Standards and Technology (NIST). *Measurement science roadmap for metal-based additive manufacturing*. U.S.: Department of Commerce - Workshop Summary Report. 2013
4. America Makes, Retrieved 08/04/2016. Technology Roadmap, , https://www.americamakes.us/technology/techroadmap.
5. Manogharan G. *CAM-IT workshop #2 report: 1) material property enhancement and 2) system integration, Consortium for Advanced Hybrid Manufacturing Integrating Technologies*. 2016:1-25.
6. Conner B, Ziegert J, Liou F, Jones J, Srinivasan H. *CAM-IT workshop #4 report: 1) inspection, qualification, and certification and 2) in-envelope hybrid, Consortium for Advanced Hybrid Manufacturing Integrating Technologies*. 2017:1-43.
7. Sealy MP, Madireddy G, Williams R, Rao P, Toursangsaraki M. Hybrid processes in additive manufacturing. J Manuf Sci Eng 2018;140. (p. 060801:1-13).
8. Sealy MP, Hadidi H, Kanger CJ, Yan XL, Cui B, McGeough JA. Glocal integrity in 420 stainless steel by asynchronous laser processing. CIRP Ann 2019https://doi.org/10.1016/j.cirp.2019.04.105.
9. ISO/ASTM International. ISO/ASTM 52900:2015 (E) standard terminology for additive manufacturing - general principles - terminology. Committee F42 on Additive Manufacturing Technologies 2016:1-9.
10. Manvatkar VD, Gokhale AA, Jagan Reddy G, Venkataramana A, De A. Estimation of melt pool dimensions, thermal cycle, and hardness distribution in the laser-engineered net shaping process of austenitic stainless steel. Metall Mater Trans A 2011;42:4080-7.
11. Wang L, Felicelli S. Analysis of thermal phenomena in LENS™ deposition. Mater Sci Eng A 2006;435–436:625-31.
12. Heigel JC, Michaleris P, Reutzel EW. Thermo-mechanical model development and validation of directed energy deposition additive manufacturing of Ti–6Al–4V. Addit Manuf 2015;5:9-19.
13. Wang L, Felicelli SD, Pratt P. Residual stresses in LENS-deposited AISI 410 stainless steel plates. Mater Sci Eng A 2008;496:234-41.
14. Wang, Q., Li, J., Gouge, M., Nassar, A.R., (Pan) Michaleris, P., Reutzel, E.W., 2016. Physics-based multivariable modeling and feedback linearization control of melt-pool geometry and temperature in directed energy deposition, journal of manufacturing science and engineering 139, p. 021013-021013-12.
15. Ye R, Smugeresky JE, Zheng B, Zhou Y, Lavernia EJ. Numerical modeling of the thermal behavior during the LENS® process. Mater Sci Eng A 2006;428:47-53.
16. Chiumenti M, Lin X, Cervera M, Lei W, Zheng Y, Huang W. Numerical simulation and experimental calibration of additive manufacturing by blown powder technology. Part I: thermal analysis. Rapid Prototyp J 2017;23:448-63.
17. Vasinonta A, Beuth JL, Griffith M. Process maps for predicting residual stress and melt pool size in the laser-based fabrication of thin-walled structures. J Manuf Sci Eng 2006;129:101-9.
18. Neela V, De A. Three-dimensional heat transfer analysis of LENS™ process using finite element method. Int J Adv Manuf Technol 2009;45:935.
19. Peyre P, Aubry P, Fabbro R, Neveu R, Longuet A. Analytical and numerical modeling of direct metal deposition laser process. J Phys D Appl Phys 2008;41:1-10.
20. Zecovic S, Dwivedi R, Kovacevic R. In: University of Texas-Austin, ed. Thermo-mechanical finite element analysis of direct laser metal deposited thin-walled structures, Solid Free Form Fabrication Symposium; 2005. p. 338-55.
21. Anca A, Fachinotti VD, Escobar-Palafox G, Cardona A. Computational modelling of shaped metal deposition. Int J Numer Methods Eng 2011;85:84-106.
22. Chiumenti M, Cervera M, Salmi A, Agelet de Saracibar C, Dialami N, Matsui K. Finite element modeling of multi-pass welding and shaped metal deposition processes. Comput Methods Appl Mech Eng 2010;199:2343-59.
23. Jendrzejewski R, Śliwiński G, Krawczuk M, Ostachowicz W. Temperature and stress fields induced during laser cladding. Comput Struct 2004;82:653-8.
24. Plati A, Tan J, Golosnoy I, Persoons R, van Acker K, Clyne T. Residual stress generation during laser cladding of steel with a particulate metal matrix composite. Adv Eng Mater 2006;8:619-24.
25. Qi H, Mazumder J, Ki H. Numerical simulation of heat transfer and fluid flow in coaxial laser cladding process for direct metal deposition. J Appl Phys 2006;100, 024903.
26. Pavelic V, Tanbakuchi R, Uyehara OA, Myers PS. Experimental and computaed thermal histories in GTA welding of thin plates. Weld J 1969;48:295-305.
27. Koster WP, Field M, Kohls JB, Fritz LJ, Gatto LR. *Manufacturing methods for surface integrity machined structural components AD0893765*. 1972:451.
28. Denlinger ER, Heigel JC, Michaleris P. Residual stress and distortion modeling of electron beam direct manufacturing Ti-6Al-4V. Proceedings of the IMechE, Vol. 229. ; 2015. p. 1803-13.
29. Yang Y, Babu SS. An integrated model to simulate laser cladding manufacturing process for engine repair applications. Weld World 2010;54:R298-307.
30. Costa L, Vilar R, Reti T, Deus AM. Rapid tooling by laser powder deposition: process simulation using finite element analysis. Acta Mater 2005;53:3987-99.
31. Marimuthu S, Clark D, Allen J, et al. Finite element modelling of substrate thermal distortion in direct laser additive manufacture of an aero-engine component. Proc IMechE 2013;227:1987-99.
32. Ghosh S, Choi J. Three-dimensional transient finite element analysis for residual stresses in the laser aided direct metal/material deposition process. J Laser Appl 2005;17:144-58.

33. Aggarangsi P, Beuth JL, Griffith M. In: University of Texas-Austin, ed. Melt pool size and stress control for laser-based deposition near a free edge, Solid Free Form Fabrication Symposium; 2003. p. 196-207.
34. Dobranich D, Dykhuizen RC. Scoping thermal calculation of the LENS™ process. Sandia National Laboratories internal report; 1998.
35. Zhang W, Yao YL. Micro scale laser shock processing of metallic components. J Manuf Sci Eng 2002;124:369-78.
36. Sealy MP, Guo YB. Fabrication and finite element simulation of micro-laser shock peening for micro dents. Int J Comput Methods Eng Sci Mech 2009;10:134-42.
37. Peyre P, Berthe L, Scherpereel X, Fabbro R, Bartnicki E. Experimental study of laser-driven shock waves in stainless steel. J Appl Phys 1998:5985-92.
38. Peyre P, Fabbro R, Merrien P, Lieurade HP. Laser shock processing of aluminium alloys. Application to high cycle fatigue behaviour. Mater Sci Eng A 1996;210:102-13.
39. Devaux D, Fabbro R, Tollier L, Bartnicki E. Generation of shock waves by laser-induced plasma in confined geometry. J Appl Phys 1993;74:2268-73.
40. Berthe L, Fabbro R, Peyre P, Tollier L, Bartnicki E. Shock waves from a water-confined laser-generated plasma. J Appl Phys 1997;82:2826-32.
41. Fabbro R, Fournier J, Ballard P, Devaux D, Virmont J. Physical study of laser-produced plasma in confined geometry. J Appl Phys 1990;68:775-84.
42. Wu B, Shin YC. A self-closed thermal model for laser shock peening under the water confinement regime configuration and comparisons to experiments. J Appl Phys 2005;97:1-11.
43. Braisted W, Brockman R. Finite element simulation of laser shock peening. Int J Fatigue 1999;21:719-24.
44. Voothaluru R, Richard Liu C, Cheng GJ. Finite element analysis of the variation in residual stress distribution in laser shock peening of steels. J Manuf Sci Eng 2012;134:061010.
45. Sealy MP, Madireddy G, Li C, Guo YB. Finite element modeling of hybrid additive manufacturing by laser shock peening, 2016 Annual International Solid Freeform Fabrication Symposium, p. 306–316; 2016.
46. Bammann DJ, Chiesa ML, Horstemeyer MF, Weingarten LI. *Failure in ductile materials using finite element methods, structural crashworthiness and failure*. 1993:1-54.
47. Bammann DJ, Chiesa ML, Johnson GC. Modeling large deformation and failure in manufacturing processes. 19th International Congress on Theoretical and Applied Mechanics T. Tatsumi, E. Watanable, T. Kambe. Amsterdam: Elsevier; 1996. p. 359-75.
48. Horstemeyer MF, Bammann DJ. Historical review of internal state variable theory for inelasticity. Int J Plast 2010;26:1310-34.
49. Ramesh A, Melkote SN. Modeling of white layer formation under thermally dominant conditions in orthogonal machining of hardened AISI 52100 steel. Int J Mach Tools Manuf 2008;48:402-14.
50. Guo YB, Liu CR. Mechanical properties of hardened AISI 52100 steel in hard machining processes. J Manuf Sci Eng 2001;124:1-9.
51. Anurag S, Guo YB, Horstemeyer MF. The effect of materials testing modes on finite element simulation of hard machining via the use of internal state variable plasticity model coupled with experimental study. Comput Struct 2009;87:303-17.
52. Shah SM, Nélias D, Zain-ul-abdein M, Coret M. Numerical simulation of grinding induced phase transformation and residual stresses in AISI-52100 steel. Finite Elem Anal Des 2012;61:1-11.

Guru Madireddy is the lead student investigator and a second year Ph.D. student in Mechanical Engineering at the University of Nebraska-Lincoln. He completed his undergraduate studies in Mechanical Engineering from Osmania University, Hyderabad, India in 2015. He received a Master of Science in Mechanical Engineering from the University of Nebraska-Lincoln in May 2018. His doctoral research focuses on ways to produce functionally gradient properties by coupling surface treatments with additive manufacturing. He is also working as assistant lab manager at the Nebraska Engineering Additive Technologies (NEAT) Lab.

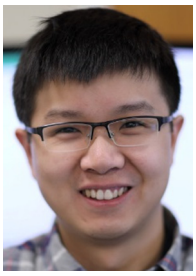

Chao Li is a Research Engineer on the Netfabb Simulation development team at Autodesk Inc. He holds a Ph.D. in mechanical engineering from the University of Alabama. His graduate research focused on manufacturing processes modeling, materials characterization, and residual stress and distortion prediction in metal additive manufacturing.

Jingfu Liu is currently the Chief Scientist of Additive Manufacturing at Sentient Science. He has expertise in the area of advanced manufacturing, metallurgical, and computational modeling. Dr. Liu obtained his Ph.D. degree of advanced manufacturing from the University of Alabama, where he conducted several researches on thermal-based manufacturing processes, including metal additive manufacturing, laser-based manufacturing, electron discharge machining, with a focus on detailing the process-microstructure-property-performance relationships for metallic materials in aerospace and medical application. Dr. Liu has been dedicated to developing viable solutions to address current roadblocks in advanced manufacturing area and commercialize early-stage R&D works in industrial applications. He has solicited over $1.3 million research funding as principal investigator to commercialize cutting-edge technique related to metal additive manufacturing. Dr. Liu has published 25+ peer-review papers and made 15+ conference presentations in advanced manufacturing community. He is also a technical reviewer of several academic journal and is an active member of TMS and SAE.

Michael P. Sealy is an Assistant Professor in Mechanical and Materials Engineering at the University of Nebraska-Lincoln. His primary research field is advanced manufacturing. He received his Ph.D in Mechanical Engineering at the University of Alabama in 2014. He investigates the role manufacturing processes have on process signature, surface integrity, and functional performance. More specifically, he is currently investigating coupling additive manufacturing with surface treatment technology on metals and polymers to print functional 3D mechanical properties for aerospace, biomedical, and automotive applications.